Design and Development of High-Performance Torque-Controlled Joints

Dieter Vischer, *Member, IEEE*, and Oussama Khatib, *Member, IEEE*

Abstract— Dynamic decoupling, motion and force control of manipulators rely on the ability of the actuation system to provide accurate joint torques. However, this ability is considerably restricted by the nonlinearities and friction inherent in the actuator-transmission systems of most industrial robots. This paper is concerned with the development of high-performance torque controlled joints and focuses on two basic issues: sensor design and torque control. The first part of the paper describes a conceptually new type of torque sensor that uses *contactless* inductive transducers. The new sensor provides a substantial increase in accuracy over conventional strain gauge sensors, achieves higher mechanical robustness, and presents lower sensitivity to electrical noise. The second part of the paper presents an analysis of the effect that the manipulator's transmission and structural properties have on the joint torque controller design. Two manipulators with very different mechanical characteristics are used in this analysis: the PUMA 560 manipulator and Artisan, an eleven-degree-of-freedom manipulator currently under development at Stanford. The experimental results obtained with a prototype link of Artisan are presented and compared to those previously obtained with the PUMA.

I. INTRODUCTION

THE research we report here is part of a larger effort to develop the technology for a new generation of force-controlled robot systems. The goal is to overcome the deficiencies inherent in conventional robots and to provide the capabilities needed for carrying out dextrous manipulation tasks. This effort has resulted in the design of Artisan, an eleven-degree-of-freedom manipulator with an integrated mini-manipulator system currently under development at Stanford University [9]. High-performance joint-torque control, optimal dynamic characteristics, motion redundancy, fine manipulation ability, and integrated sensing are among the basic characteristics of this robot. In this paper, the discussion focuses on two basic issues associated with the development of high-performance torque-controlled joints: torque sensor design and joint torque control.

Typical manipulators transmit actuator torques to the joints through gear systems with high gear ratios. These gear systems are prone to nonlinearities such as cogging, backlash, and various types of friction. Actuator-transmission nonlinearities have a considerable effect on the ability to control manipulator joint torques. In the last fifteen years, there have been several

D. Vischer was with the Robotics Laboratory, Department of Computer Science, Stanford University. He is now with ESEC SA, Cham, Switzerland.
O. Khatib is with the Robotics Laboratory, Department of Computer Science, Stanford University, Stanford, CA 94305 USA.

attempts to improve joint torque control through the use of joint torque feedback. Based on experiments with a single joint [16], the first two joints of a Stanford Arm were redesigned [10] to accommodate torque sensors. Joint torque sensory feedback has also been implemented in a direct-drive manipulator [3] and in a PUMA manipulator [11]. Torque sensors are today integrated in some commercial manipulators, such as the modular arm developed by Robotics Research, which uses harmonic drive reducers and joint torque feedback control. These developments have shown that, although joint friction effects can be reduced by torque servoing, higher performance in the control of joint torques is difficult to achieve without actually reducing the friction and nonlinearities in the actuator-transmission system.

Another line of research has been directed at the development of direct-drive arms. Since the development of the first direct-drive arm at CMU in 1981 [2], several other designs have been proposed and direct-drive manipulators have become commercially available. While avoiding transmission nonlinearities, direct drive manipulators become increasingly massive and bulky as the number of degrees of freedom increases. Additionally, direct-drive manipulators are more sensitive to dynamic coupling than high gear-ratio manipulators, and thus are more susceptible to dynamic modeling errors and dynamic perturbations.

The list of desirable properties for a torque controlled joint includes: high backdriveability, low friction, minimal effects of ripple torques and dynamic forces, high ratio of torque capacity to torque accuracy, low backlash, and small distributed elasticities between sensor and actuator [4], [5].

These desirable characteristics clearly point toward transmissions with low gear ratios. The solution we have adopted for the actuation of Artisan has been to combine a single-stage, low gear ratio transmission system with joint torque feedback control. With this type of transmission, the friction and other nonlinear effects are minimized. These effects are further reduced by the joint torque feedback compensation.

The first part of the paper is devoted to the description of the new torque sensor. In the second part, we discuss the basic characteristics of torque controlled joints, where high versus low gear-ratio and rigid versus compliant manipulators will be compared.

II. PROTOTYPE LINK

The prototype link for Artisan is shown in Fig. 1. It uses a brushless DC motor, mounted at the base of the link in order to counterbalance the link's weight. The motor torque
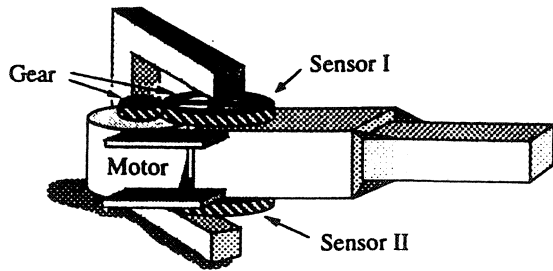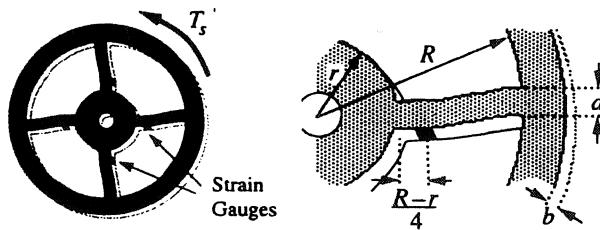
Fig. 1. Prototype link

Fig. 2. Strain gauge sensor.

Fig. 3. Sensor placement.

is transmitted in parallel through two single-stage helical[1] low gear-reduction transmissions. The torque sensor is integrated with the gear. A shaft encoder is located on the motor axis to measure the relative position between the link and the motor.

III. NEW TORQUE SENSOR DESIGN

Breakaway friction for high gear-ratio manipulators with brush type servo-motors such as the PUMA is usually much higher (more than an order of magnitude) than the friction resulting from the brushless dc motors of the low gear-ratio prototype of Artisan. To reduce the already low friction, high torque accuracy is needed for the sensor of the prototype. The breakaway torque we have measured for the open-loop system was in the range of 0.5% of the maximum torque. This breakaway torque is strongly dependent on the link angle, because of eccentricities in the gear system. To substantially reduced the effect of this breakaway torque, we estimated the required resolution (torque accuracy to maximum torque) of the sensor to be in the range of 0.03%. Building a sensor with such a resolution is not an easy task in practice.

A. Strain Gauge Sensors

We have first used the four beam torque sensor shown in Fig. 2. Beam deflection is measured by semiconductor strain gauges. The torsional stiffness k'_s and the strain ε at the gauge location can be found as

$$k'_s = \frac{4Ea^3b(R^2 + Rr + r^2)}{3(R - r)^3};$$ (1)

$$\varepsilon = \frac{3(R - r)(5R + r)}{16Ea^2b(R^2 + Rr + r^2)}T'_s$$ (2)

where E is the Young's modulus. Eight strain gauges arranged in Wheatstone bridges were used for each of the two sensors integrated in the two gears.

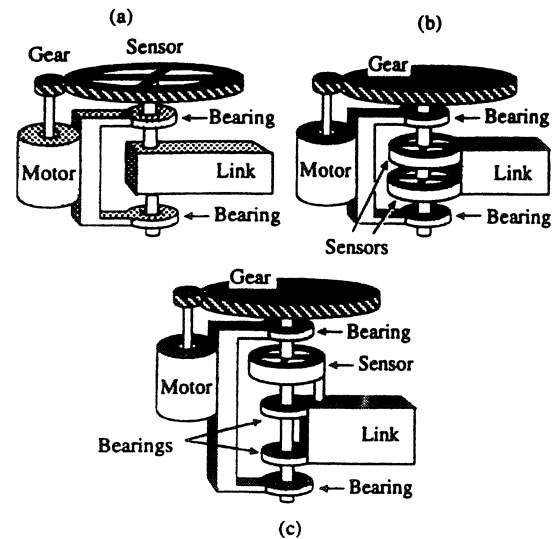[1] Evoloid gears have been used in subsequent prototypes.

With this type of sensor, gear eccentricities have been shown to result in a position-dependent torque offset which was 5 to 10 times higher than the required accuracy. The use of lookup tables to compensate for this dependency resulted in significant improvements but did not allow us to obtain the required resolution of 0.03%.

B. Sensor Placement

In the initial design of the prototype link, the sensor was placed in the gear as shown in Fig. 3(a). With this arrangement, the sensor is not sensitive to those dynamic forces or contact forces acting on the link, which do not contribute to the joint torque. At that location, however, the sensor is exposed to large radial forces caused by the transmission system. We have found and experimentally verified that very small eccentricities in the gear (10^{-5} to 10^{-6} m) could result in radial forces high enough to saturate (and sometimes break) the strain gauges.

An alternative to this initial design (Fig. 3(a)) is shown in Fig. 3(b). In this configuration the sensors are exposed to dynamic and contact forces that do not contribute to the joint torque but are protected from the much larger radial forces due to eccentricities of the gear.

This second design has been used later in the development of a prototype of two links of Artisan [8]. Further improvements in sensor disturbance protection can be achieved by using the configuration shown in Fig. 3(c). A second set of bearings is used to better protect the sensor from disturbances. Although significant improvements can be obtained by careful sensor design, radial forces cannot be entirely suppressed.

C. Modeling of Radial Forces

The effect of radial forces acting on each individual gauge can be formulated as a mechanical signal-to-noise ratio, as shown in Fig. 4.

The strain ε_{noise} caused by the radial force F_r depends on the direction of F_r. It can be shown that ε_{noise} reaches its maximum when F_r is parallel to the beam. The minimal
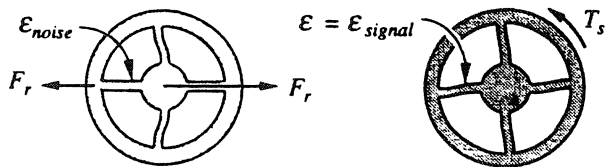
Fig. 4. Signal-to-noise ratio.

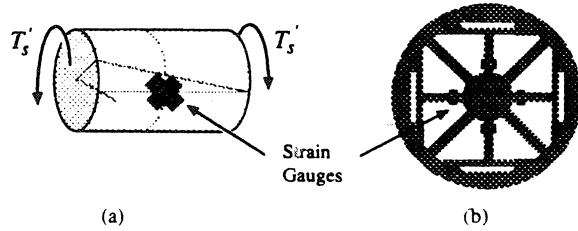(a)   (b)

Fig. 5. Torque sensor designs.

Fig. 6. New torque sensor.

signal-to-noise ratio (worst case) can be calculated as

$$\frac{\varepsilon_{\text{signal}}}{\varepsilon_{\text{noise}}} = \gamma \frac{T'_s}{F_r}; \tag{3}$$

with

$$\gamma = \frac{3(5R + r)((R - r)^2 + a^2)}{8a(R - r)(R^2 + Rr + r^2)}. \tag{4}$$

The factor γ depends only on the geometry of the sensor. Since a 10 to 20 times increase of γ would provide the needed accuracy, we focused our effort on designs that would maximize the value of γ. We have also analyzed the signal-to-noise ratio characteristics for other sensor configurations, as shown in Fig. 5.

Fig. 5(a) shows a torsional sensor as describe by Wu and Paul [16]. Those sensors have high robustness to radial forces, but are quite sensitive to torque disturbances in other directions. Fig. 5(b) shows an eight beam sensor. Although adding beams improves the signal-to-noise ratio, the manufacturing difficulty and sensor cost increase rapidly.

D. New Torque Sensor

The design concept of the new sensor is illustrated in Fig. 6. Torques are obtained from measurements of the beam deflections using four contact-free displacement sensors. The basic idea is that contact-free sensors only measure changes in the gap, e.g., perpendicular to the surface of the sensor, whereas parallel movements do not result in measurement changes. A deflection due to radial forces cannot be entirely prevented. However, it is possible to build a sensor where radial forces mostly result in deflections parallel to the sensor's surface and thus have little contribution to the measurement. This is the case for the sensor shown in Fig. 6.

To show the lower sensitivity to radial forces of the new sensor compared to conventional strain gauge sensors, we derive the signal to noise ratio of the new sensor. The deflection at the sensor can be evaluated as
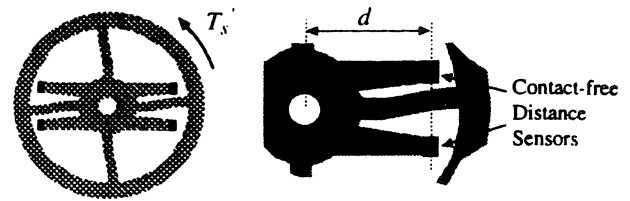
$$\Delta x = \Delta x_{\text{signal}}. \tag{5}$$

A radial force, F_r, will result in a deflection $\Delta x = \Delta x_{\text{noise}}$, which depends on the direction of F_r. Δx_{noise} reaches its maximum when F_r is parallel to the measured deflection. The minimal signal-to-noise ratio (worst case) is

$$\frac{\Delta x_{\text{signal}}}{\Delta x_{\text{noise}}} = \gamma \frac{T'_s}{F_r} \tag{6}$$

with

$$\gamma = \frac{3d((R - r)^2 + a^2)}{2a^2(R^2 + Rr + r^2)}. \tag{7}$$

By comparing (3), (4) and (6), (7) the advantage of the contact-free sensor over strain gauge based sensing can now be verified.

There are various types of contact-free displacement sensors such as optical, capacitive, eddy current and inductive sensors. For our application, it was necessary to use sensors with a resolution better than a micrometer in order to build a stiff torque sensor. Furthermore, high mechanical robustness as well as low sensitivity to electrical noise was required. Both inductive and eddy-current sensors have the necessary properties.

An inductive sensor is basically an electromagnet. The inductance of its coil changes with varying air gap and is measured with a high frequency signal usually in the range of 1 to 20 kHz. If higher frequencies of 50 to 500 kHz are used to modulate the sensor, it can be observed that the changes of the inductance due to the varying air gap are no longer significant. At this frequency range, it is more appropriate to measure changes of the real part of the impedance resulting from eddy currents. This type of sensor is called an "eddy-current sensor." It provides a very high resolution, even in electrically noisy environments. Since we wanted to use a commercially available sensor having a compact housing, we decided to employ an inductive sensor that is almost as good in terms of resolution and noise rejection as an eddy-current sensor.

The final layout of the new sensor is shown in Fig. 7. It uses a six beam structure with four inductive transducers arranged in a Wheatstone bridge configuration. The signal-to-noise ratio of the new sensor is 24 times greater than the value obtained with the initial sensor ($\gamma = 1730$ m^{-1}).

E. Mechanical Robustness and Electrical Noise

The signal-to-noise ratio is an important parameter in the design of a torque sensor. However, the new torque sensor has other advantages, that for some applications, might be even more useful than its high resolution.
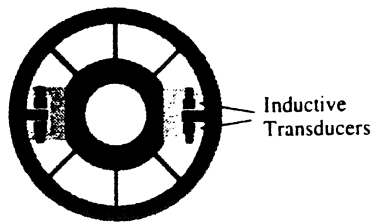
Fig. 7.   Torque sensor layout.

Strain gauges are quite fragile and tend to break easily. Their maximum allowable strain is fairly close to the strain at which they break, making failure prevention difficult. The protection of torque sensors from overloads generally relies on the use of mechanical stops that limit the deflections in the sensor structure. Because of stiffness requirements, these deflections are very small. Very precise machining is therefore needed to manufacture these mechanical stops. The sensor has to be protected not only against torque overloads but also against radial and other force components.

The new torque sensor has been designed in such a way that the largest torque to be measured corresponds to the largest possible deflection in the linear range of the inductive sensors. This means that even when the largest torque is applied, there is still an air-gap of more than a tenth of a millimeter.

With inductive sensors, mechanical limits are much simpler to design and build. For each sensor, only one overload stop was needed for protection against all possible torques and forces acting on the torque-sensor. The inductive sensors we use are housed in steel cases and our torque-sensor can thus withstand torques that are much higher than the maximum torque, even without the mechanical limits.

Inductive sensors are also easy to mount and replace, whereas mounting strain gauges (especially semiconductor ones) involves a lengthy procedure that requires expertise. Another shortcoming of strain gauges is their sensitivity to electrical noise. Although their resolution (ratio of minimal to maximal measurable strain) is very high (better than 0.003% for semiconductors), this precision can only be reached in an environment free of noise. With the new sensor, the inductive bridge is modulated with a carrier frequency of 5 kHz. This significantly reduces the sensitivity to electrical noise.

The linearity of the torque-sensor depends on both the linearity of the inductive sensors (better than 0.05% of full scale) and the linearity of the deflecting structure. The bandwidth of the inductive sensors we used was about 1 kHz. This was much higher than needed in our application.

IV. JOINT TORQUE CONTROL

Joint torque performance depends not only on the accuracy and bandwidth of the torque-sensor but also on the gains achievable by the controller. A better understanding of the limitations placed on these gains has been one of the objectives in our experiments with the prototype link.

A. Model of the Prototype Link

The parameters of the prototype link for Artisan (Fig. 1) are given in Table I.

TABLE I
LINK PARAMETERS

N	Gear Ratio	m	Motor Mass
$\bar{J}_l$	Link Inertia	J_m	Motor Inertia
d_l	Link Friction	d_m	Motor Friction
T_s	Sensor Torque	T_m	Motor Torque
θ_l	Link Angle	θ_m	Motor Angle

The equations of motion of the link involve additional dynamic forces resulting from the rotation of the motor relative to the link. During a full revolution of the link, the motor makes $N + 1$ turns with respect to the inertial frame:

$$T_m - \frac{T_s}{N} = J_m(\ddot{\theta}_m + \ddot{\theta}_l) + d_m\dot{\theta}_m \tag{8}$$

$$T_s(1 + \frac{1}{N}) - T_m = (\bar{J}_l + ml^2)\ddot{\theta}_l + d_l\dot{\theta}_l - d_m\dot{\theta}_m \tag{9}$$

where l is the distance between the joint axis and motor axis. The two torque sensors and the transmission can be modeled as a linear spring with total stiffness k_s:

$$T_s = k_s\theta_s \tag{10}$$

where θ_s is the angle of sensor deflection

$$\theta_s = \frac{\theta_m}{N} - \theta_l. \tag{11}$$

B. Torque Transfer Function

The transfer function of motor torque T_m to sensed torque T_s (which corresponds to the joint torque) can be obtained from (1), (9), (10), and (11) as

$$\frac{T_s}{T_m} = \frac{b_1 s + b_0}{s^3 + a_2 s^2 + a_1 s + a_0} \tag{12}$$

with

$$a_0 = \frac{k_s}{J_m J_l}(\frac{d_l}{N^2} + d_m) \tag{13}$$

$$a_1 = \frac{k_s}{N^2 J_m J_l}(J_l + (N + 1)^2 J_m) + \frac{d_l d_m}{J_m J_l} \tag{14}$$

$$a_2 = \frac{d_m}{J_m} + \frac{d_l}{J_l} + \frac{d_m}{J_l} \tag{15}$$

$$b_0 = \frac{d_l k_s}{N J_m J_l} \tag{16}$$

$$b_1 = \frac{k_s}{N J_m J_l}(J_l + (N + 1)J_m) \tag{17}$$

and

$$J_l = ml^2 + \bar{J}_l. \tag{18}$$

The transfer function for the free link is third order with two complex poles, a negative real pole, and a negative real zero. The transfer function for the constrained link can be found from (12) by letting J_l go to infinity:

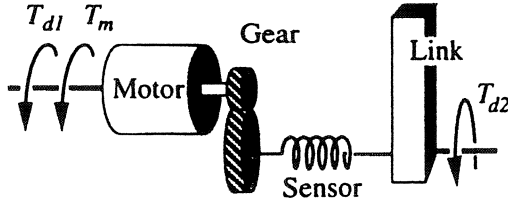$$\frac{T_s}{N T_m} = \frac{\omega_0'^2}{s^2 + 2\xi_0'\omega_0' s + \omega_0'^2} \tag{19}$$

Fig. 8. Approximate model with disturbance torques.

with

$$\xi_0' = \frac{d_m}{2\omega_0' J_m} \text{ and } \omega_0'^2 = \frac{k_s}{N^2 J_m}. \tag{20}$$

This shows the constrained link to have a second order behavior. In fact, the free link can be also characterized by a second order dominant behavior.

Examination of (12) shows that the free link's transfer function reduces to a second order function, when the values of both the link viscous friction, d_l, and the motor viscous friction, d_m, are zero.

One of the main objectives in the design of Artisan has been to reduce the friction in the actuation transmission systems. Brushless motors, one-stage low gear ratio transmissions, and careful mechanical design all contributed to low friction in the prototype link. This was experimentally verified, as frequency and step responses have shown the friction effects to be fairly low for this prototype (see Fig. 14). These experiments have also shown the link's dominant second order behavior.

In the following, we will use the second order transfer function associated with $(d_l = d_m = 0)$ to represent the dominant behavior of the free link. By setting $d_m = d_l = 0$, (12) is reduced to

$$\frac{T_s}{NT_m} = \frac{k_0\omega_0^2}{s^2 + \omega_0^2} \begin{cases} k_0 = \frac{(N+1)J_m+J_l}{(N+1)^2 J_m + J_l} \le 1 \\ \omega_0^2 = k_s \frac{(N+1)^2 J_m + J_l}{N^2 J_m J_l} \end{cases} \tag{21}$$

where k_0 is the open-loop gain and $\omega_0/2\pi$ is the open-loop frequency, f_0. Observing that $N \gg 1$ and $J_l \gg N J_m$. the parameters k_0 and ω_0 can be further simplified to

$$k_0 = \frac{1}{1 + \frac{N^2 J_m}{J_l}} \tag{22}$$

$$\omega_0^2 = k_s\left(\frac{1}{J_l} + \frac{1}{N^2 J_m}\right). \tag{23}$$

Equations (22) and (23) correspond to a link with an inertia J_l driven by a motor that is fixed in the inertial frame, as shown in Fig. 8.

C. Disturbances

Static friction (Coulomb friction), kinetic friction, and motor ripple torques can be regarded as disturbance torques acting on the motor. The sensed torque is also affected by other disturbances originating at the link, such as friction in the gears and dynamic forces resulting from the action of other links or from link interaction with the environment.

Some of these effects can be modeled, identified, and compensated for in the control algorithm. Armstrong [1] has

TABLE II
PROTOTYPE AND PUMA PARAMETERS

	Prototype	PUMA
Gear Ratio, N	6	53.7
$\frac{N^2 J_m}{J_l}$	0.12	2.5
Motor Inertia, J_m	0.000755 kg m^2	0.000288 kg m^2
Link Inertia, J_l	0.23 kg m^2	0.336 kg m^2

TABLE III
OPEN-LOOP CHARACTERISTICS

		Prototype	PUMA
Gain, k_0	Link Free	0.88	0.29
	Link Fixed	1	1
Frequency, f_0	Link Free	90 Hz	41 Hz
	Link Fixed	85 Hz	22 Hz
Disturbance (Link Free)	$\frac{T_s}{T_{d1}}\vert_{s=0}$	5.28	15.6
	$\frac{T_s}{T_{d2}}\vert_{s=0}$	0.18	0.73

shown the effectiveness of feedforward compensations using look-up tables. Our goal is to couple feedforward compensation with joint torque feedback to greatly reduce unmodeled disturbances and add robustness to modeling errors. Unknown disturbances and model errors can be grouped into two classes:

• T_{d1} : the sum of disturbances originating at the motor;
• T_{d2} : the sum of disturbances acting at the link.

The transfer function (with $d_l = d_m = 0$) then becomes

$$T_s = \frac{k_0\omega_0^2}{s^2 + \omega_0^2}(NT_m + T_d): \tag{24}$$

with

$$T_d = NT_{d1} + \frac{N^2 J_m}{J_l}T_{d2}. \tag{25}$$

Equations (24) and (25) describe the influence of disturbances on the open-loop system (see Fig. 8). An advantage of low gear-ratio robots such as Artisan is that their open-loop characteristics, k_0 and f_0, are less sensitive to changes in the link inertia, J_l. In addition, sensed torques are less sensitive to the disturbance torque, T_{d2}, acting at the link ((24) and (25)). This is illustrated in the following two examples.

D. Open-Loop Characteristics: Examples

Pfeffer, Khatib, and Hake [11] have developed a joint torque sensory feedback controller for the third link of a PUMA 560 manipulator. The PUMA 560 is an example of a relatively high geared manipulator with low open-loop frequency. Here, it is used to provide a basis for a comparison with the low geared and comparatively rigid prototype link of Artisan.

The relevant parameters for the Artisan prototype and the PUMA are shown in Table II. The open-loop characteristic for the two examples, obtained from (21), (19), (24), and (25), are summarized in Table III. The data in this Table illustrates the advantages of low over high gear-ratio manipulators discussed above.
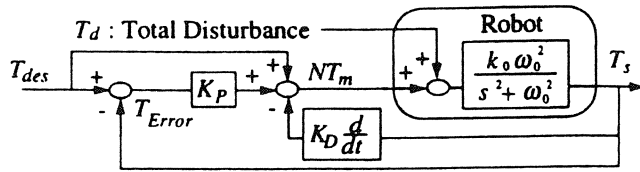
Fig. 9. PD controller.

Fig. 10. Approximate model with disturbance torques.

Fig. 11. Required motor torque.

E. Torque Controller Design

The type of joint-torque controller that is most suitable for a given manipulator is strongly dependent on the manipulator open-loop characteristics. Various PID and lead-lag controller designs have been used in the development of joint torque control systems. To discuss the impact of the open-loop characteristics on the suitability and limitations of controller designs, we will use simple PID controllers. The disturbance rejection and robustness of lead-type controllers will be analyzed using PD controllers, while integral-type controllers will be used to discuss the dominant characteristics of lag-type designs.

The control law of a PD controller (see Fig. 9) is

$$NT_m = T_{des} - K_P(T_s - T_{des}) - K_D \dot{T}_s \qquad (26)$$

where K_P and K_D are the proportional and derivative feedback gains, respectively. The input feedforward reduces static errors.

The closed-loop transfer function can be obtained from (24), (25), and (26) as

$$T_s = \frac{k_c \omega_c^2}{s^2 + 2\xi_c \omega_c s + \omega_c^2}(T_{des} + \frac{T_d}{K_P + 1}) \qquad (27)$$

where the closed-loop gain k_c, damping ratio ξ_c and frequency f_c are

$$k_c = \frac{1}{1 + \frac{J_m^*}{J_l}}: \qquad (28)$$

$$\xi_c = \frac{K_D k_0 \omega_0^2}{2\omega_c}: \qquad (29)$$

$$\omega_c^2 = k_s(\frac{1}{J_m^*} + \frac{1}{J_l}). \qquad (30)$$

with

$$J_m^* = \frac{N^2 J_m}{K_P + 1}. \qquad (31)$$

The transfer function associated with the closed-loop system is similar to that of the open-loop. However, the link is now driven by a "motor" whose inertia is $K_P + 1$ times smaller. Disturbance torques are also $K_P + 1$ times smaller. A mechanical equivalent to the closed-loop system is shown in Fig. 10, where J_m^* is the equivalent motor inertia. Given that $J_l \gg J_m^*$, the closed-loop parameters can be approximated as

$$k_c \approx 1 \text{ and } \omega_c^2 \approx \frac{k_s}{J_m^*} = k_s \frac{K_P + 1}{N^2 J_m}. \qquad (32)$$

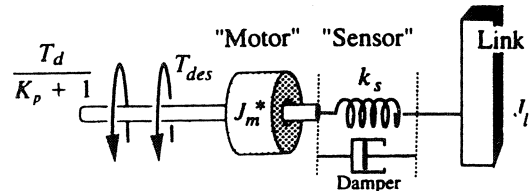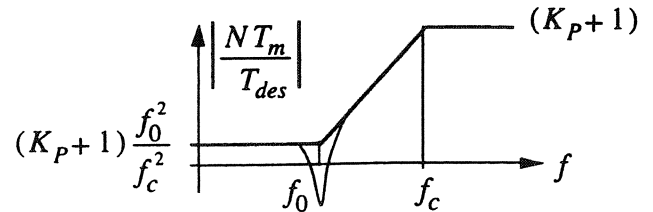With $K_D > 0$, equations (27), (28), (29), (30), and (31) show the closed-loop system to be stable for all gains $K_P > -1$. For gains between -1 and 0, disturbances are amplified. Thus, in order to achieve an improvement over the open-loop system, these gains must be larger than zero. This also means that the closed-loop frequency f_c must be larger than the open-loop frequency f_0.

Equation (32) provides a basis for trade-offs between achievable disturbance rejection $K_P + 1$, closed-loop bandwidth f_c, and sensor stiffness k_s. This equation (32) also shows that in the case of lead-type control, a lower sensor stiffness corresponds to a higher disturbance rejection for a given achievable bandwidth, as observed by Roberts [12] and Whitney [15].

While a low sensor stiffness is desirable ((32)) to achieve larger gains and better disturbance rejection, high gains result in increased motor activity. Higher motor torques will then be needed to counter the lower rigidity of the system. The transfer function of desired torque to motor torque is

$$NT_m = \frac{(K_P + 1)(s^2 + \omega_0^2)}{s^2 + 2\xi_c \omega_c s + \omega_c^2}T_{des}. \qquad (33)$$

The Bode diagram of this transfer function (see Fig. 11) shows that changes in the desired torque at frequencies greater than f_0 will require up to $K_P + 1$ times greater actuator torques. Below f_0 the required actuator torques are comparable to those needed for a rigid link.

The Artisan link prototype is a relatively low geared system ($N^2 J_m \ll J_l$). The achievable disturbance rejection factor $K_P + 1$ in this case can be estimated as

$$K_P + 1 \approx \frac{f_c^2}{f_0^2}. \qquad (34)$$

Given the relatively high open-loop frequency of the link prototype (90 Hz), any reasonable disturbance rejection factor will result in a relatively high requirement on achievable closed-loop frequency. For instance, a reduction factor of 95% corresponds to a closed-loop frequency of about 400 Hz. This would be clearly much too high of a frequency, considering the bandwidth limitations for such a mechanism [14]. The most constraining factor on the closed-loop bandwidth, f_c, is caused by the lowest unmodeled structural mode in the system.
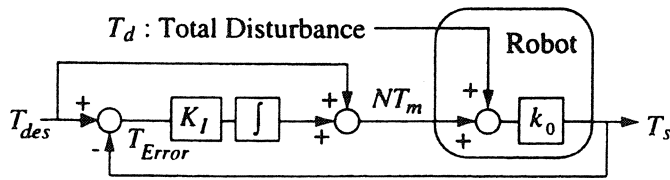
Fig. 12. Integral controller.

Fig. 13. Disturbance rejection.

The upper bound on the achievable closed-loop frequency for such a system of noncollocated actuator/sensor is generally estimated [5], [6] at a third of the first unmodeled structural mode.

Because of its lower open-loop frequency, the PUMA link places a much lower requirement on the closed-loop bandwidth than that needed for the prototype link of Artisan. The closed-loop frequency for the PUMA link is estimated at $f_c = 100$ Hz corresponding to a gain, K_P, of 19 ((32)). This results in a 95% reduction in the effective friction $(1 - (1/(K_P + 1)))$, and a significant reduction of the effective inertia of the motor. The open-loop high geared PUMA link $(N^2 J_m/J_l = 2.5)$ becomes similar to a low geared system with $J_m^*/J_l = 0.13$. In the actual experiment with the third link of the PUMA 560 [11], a factor of 97% has been achieved with a second order digital lead/lag controller.

F. Integral-Type Controller

Integral action provides an effective solution for the control of systems with high open-loop dynamics. This type of control has been, for instance, used for a direct drive arm [3], which exhibits an open-loop frequency of 650 Hz. Integral-type controllers have been also found suitable for the link prototype of Artisan. Ignoring the high frequencies in the open-loop system, the open-loop transfer function can be treated as

$$T_s \approx k_0(NT_m + T_d)(k_s \rightarrow \infty).$$ (35)

As shown in Fig. 12, the control law is

$$NT_m = T_{des} - K_I \int (T_s - T_{des}) dt$$ (36)

where K_I is the integral gain. The closed-loop transfer function can be obtained from (35) and (36) as

$$T_s = \frac{k_0(s + K_I)}{s + k_0 K_I} T_{des} + \frac{k_0 s}{s + k_0 K_I} T_d.$$ (37)

For low geared manipulators $(N^2 J_m \ll J_l)$ the transfer function can be further simplified to

$$T_s \approx T_{des} + \frac{s}{s + K_I} T_d.$$ (38)

With the above controller, disturbances are reduced for frequencies below $K_I/2\pi$, as shown in Fig. 13. This type of controller is independent of the stiffness of the sensor. The transfer characteristic of the closed-loop system is similar to that of a direct drive manipulator $(T_s \approx T_{des})$.
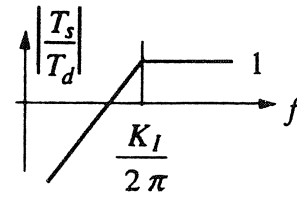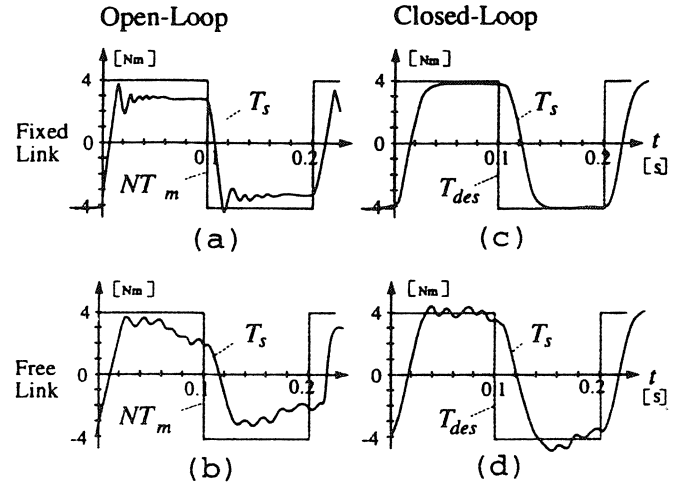

Fig. 14. Experimental results.

G. Experimental Results

Fig. 14 shows various step responses (square wave) for the prototype link.

The schematic of the controller is shown in Fig. 15. A simple lag controller was used for both the free and constrained link, with the control law

$$T_{out} = \frac{0.47z}{z - 0.997} T_{in}.$$ (39)

The Artisan prototype has little natural damping, and its open-loop frequencies are 85 Hz for the fixed link, and 90 Hz when the link is free. The open-loop responses are shown in Fig. 14(a) and (b). The 10–90% rise time for the closed-loop system (see Fig. 14(c)) is less than 15 ms. The disturbance rejection bandwidth, $K_I/2\pi$, is 30 Hz. Desired torque inputs, which are typically below the 30 Hz disturbance rejection bandwidth, are accurately controlled. The sampling frequency of the digital controller was 400 Hz. A look-up table for the position-dependent torque offset proved to be beneficial in the control of this prototype. A second order low-pass filter (bandwidth: 70 Hz, damping ratio: $\xi = 1$) for the input was used to prevent the command torque from exciting the first resonant mode at 90 Hz.

For the free link (see Fig. 14(a) and (d)), the resonant mode is excited by cogging in the transmission system. Although the controller is unable to prevent this behavior, it does significantly reduce the static errors. The ripples caused by the transmission are reduced by the output filter (70 Hz, $\xi = 1$) before being fed back to the controller. The filtering of high resonance frequencies prevents instabilities caused by phase lag in the closed-loop system at high frequencies.
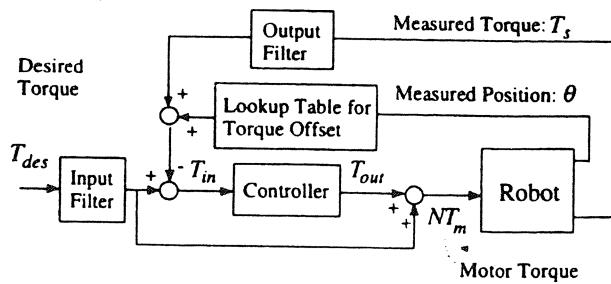
Fig. 15.   Controller schematic.

V. CONCLUSION

In this paper, we have presented the design concepts of a new type of torque sensor and discussed a number of basic issues associated with the development of joint torque control systems. The new sensor is based on contactless displacement measurements provided by inductive transducers. The signal-to-noise ratio of the new sensor has been shown to be 24 times that of conventional strain gauge sensors. In addition, the new sensor exhibits high mechanical robustness and low sensitivity to electrical noise. The effectiveness of the sensor for providing joint torque feedback has been experimentally illustrated on a prototype link of Artisan.

Our discussion of joint torque control has also addressed the impact of the manipulator mechanical characteristics on the limitations and suitability of torque controllers. Two manipulators with different characteristics have been considered: the PUMA 560 and Artisan. While PD controllers have been found compatible with the low open-loop frequency characteristic of the PUMA 560 manipulator, this type of controller proved unsuitable for the prototype link of Artisan. This link, which exhibits a relatively higher open-loop frequency, was effectively controlled with an integral-type design.

The work presented in this paper has provided the basis for the design and development of subsequent prototypes of Artisan [8], the Rotex robot [7], and several other ongoing robot design projects.

ACKNOWLEDGMENT

REFERENCES

[1] B. Armstrong, "Dynamics for robot control: Friction modeling and ensuring excitation during parameter identification," Ph.D. dissertation, Dept. of Electrical Engineering, Stanford Univ., Stanford, CA, June 1988.

[2] H. Asada and T. Kanade, "Design of direct-drive mechanical arms," ASME J. Vibration, Acoustics, Stress, and Reliability in Design, vol. 105, no. 3, pp. 312–316, 1983.

[3] H. Asada, K. Youcef-Toumi, and S. K. Lim, "Joint torque measurement of a direct drive arm," in Proc. 23d IEEE Conf. Decision and Control, 1984, pp. 1332–1337.

[4] E. Colgate and N. Hogan, "An analysis of contact instability in terms of passive physical environments," in Proc. IEEE Int. Conf. Robotics Automat., Scottsdale, AZ, 1989, pp. 404–409.

[5] S. D. Eppinger and W. P. Seering, "On dynamics of robot force control," in Proc. IEEE Int. Conf. Robotics Automat., San Francisco, CA, 1986, pp. 29–34.

[6] ——, "Understanding bandwidth limitations in robot force control," in Proc. IEEE Int. Conf. Robotics Automat., 1987, pp. 904–909.

[7] G. Hirzinger et al., "The sensory and telerobotic aspects of the space robot technology experiment Rotex," in Proc. Int. Symp. Artificial Intell., Robotics and Automation in Space, Toulouse, France, 1992, pp. 83–110.

[8] R. Holmberg, S. Dickert, and O. Khatib, "A new actuation system for high-performance torque-controlled manipulators," in Proc. RoManSy 9, CISM-IFToMM Symp. Theory and Practice of Robots and Manipulators, Udine, Italy, 1992, pp. 285–292.

[9] O. Khatib, B. Roth, and K. Waldron, "The design of a high-performance force-controlled manipulator," in Proc. 8th IFToMM World Congress on the Theory of Machines and Mechanisms, Prague, Czechoslovakia, 1991, pp. 475–478.

[10] J. Y. S. Luh, W. D. Fisher, and R. P. Paul, "Joint torque control by a direct feedback for industrial robots," IEEE Trans. Automat. Control, vol. AC-28, no. 2, pp. 153–160, 1983.

[11] L. Pfeffer, O. Khatib, and J. Hake, "Joint torque sensory feedback in the control of a PUMA manipulator," IEEE Trans. Robotics Automat., vol. 5, no. 4, pp. 418–425, 1989.

[12] R. K. Roberts, R. P. Paul, and B. M. Hillberry, "The effect of wrist sensor stiffness on the control of robot manipulators," in Proc. IEEE Int. Conf. Robotics Automat., St. Louis, MO, 1985, pp. 269–274.

[13] G. Stepan and L. Stevan, "Theoretical and experimental stability analysis of a hybrid position-force controlled robot," in Proc. RoManSy 8, CISM-IFToMM Symp. Theory and Practice of Robots and Manipulators, Cracow, Poland, July 1990.

[14] D. Vischer and O. Khatib, "Design and development of torque-controlled joints," in Experimental Robotics 1, V. Hayward and Khatib, Eds. Berlin: Springer-Verlag, 1990, pp. 271–286.

[15] D. E. Whitney, "Historical perspective and state of the art in robot force control," in Proc. IEEE Int. Conf. Robotics Automat., St. Louis, MO, 1985, pp. 883–889.

[16] C. H Wu and R. P. Paul, "Manipulator compliance based on joint torque control," in Proc. 19th IEEE Conf. Decision and Control, 1980, pp. 88–94.
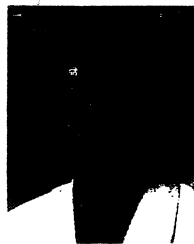
Dieter Vischer (M'86) was born in Switzerland in 1961. He received the M.S. and Ph.D. degrees in electrical engineering from the Swiss Federal Institute of Technology (ETH) in 1986 and 1988, respectively. His doctoral research was in the area of Active Magnetic Bearings.

During 1988–1989 he worked as a researcher at the Robotics Laboratory of Stanford University in the area of force and torque control of robots. Between 1989 and 1993 he was a senior research associate at ETH leading the project: "Cooperating Robot with Visual and Tactile Skills." From 1993 to 1994 he was with the engineering consultant firm, "Zuehlke," building an assembly line involving laser-welding and cutting with robots. In 1994 he joined "ESEC," a manufacturer of equipment for the semiconductor industry (die bonders and wire bonders).

Oussama Khatib (M'85) received the Ph.D. degree in 1980 from l'École Nationale Supérieure de l'Aéronautique et de l'Es-pace (Sup-Aéro), Toulouse, France.

He is an Associate Professor of Computer Science and (by courtesy) Mechanical Engineering at Stanford University. His research interests include object-level manipulation, multi-arm cooperation, mobile robotic manipulation, sensor-based strategies and compliant motion primitives, real-time collision avoidance and integrated planning and control. Addressing the limitations of current robot technology, he is also working on the design and development of a new generation of force-controlled robot manipulator systems.